Studies on Im-3-type KSbO$_3$ using high pressure X-ray diffraction and Raman spectroscopy

Huifang Zhao, Dayong Tan, Yu Tian, Yunhong He, Yanchun Li, Xiaodong Li, Ke Yang, Bin Chen & Wansheng Xiao

Published online: 20 May 2018.

Submit your article to this journal ✎

Article views: 12

View related articles ✎

View Crossmark data ✎

Taylor & Francis
Taylor & Francis Group

Check for updates

Studies on *Im*-3-type KSbO₃ using high pressure X-ray diffraction and Raman spectroscopy

HPSTAR
623-2018

Huifang Zhao[a,b], Dayong Tan[a], Yu Tian[a,b], Yunhong He[a,b], Yanchun Li[c], Xiaodong Li[c], Ke Yang[d], Bin Chen[e] and Wansheng Xiao[a]

[a]CAS Key Laboratory of Mineralogy and Metallogeny, and Guangdong Provincial Key Laboratory of Mineral Physics and Materials, Guangzhou Institute of Geochemistry, Chinese Academy of Sciences (CAS), Guangzhou, People's Republic of China; [b]University of Chinese Academy of Sciences, Beijing, People's Republic of China; [c]Institute of High Energy Physics, Chinese Academy of Sciences, Beijing, People's Republic of China; [d]Shanghai Synchrotron Radiation Facilities, Shanghai Institute of Applied Physics, Chinese Academy of Sciences, Shanghai, People's Republic of China; [e]Center for High Pressure Science and Technology Advanced Research, Shanghai, People's Republic of China

ABSTRACT

In situ X-ray diffraction and Raman scattering experiments using a diamond anvil cell revealed that *Im*-3-type KSbO₃ remains stable up to 40.5 GPa with a bulk modulus $K_0 = 101.6$ (7) GPa. Rietveld structure refinements and mode Grüneisen parameters suggested that the stability mechanism of this three-dimensional cubic tunnel structure was attributed to the isotropic compression for all types of Sb–O bonding in the unit of SbO₆ octahedron. Isotropic structure adjustment with external pressure reflected the nature that *Im*-3-type KSbO₃ model structure has a high ionic tolerance with a change in the chemical pressure in the isomorphous substitutions.

1. Introduction

Isomorphous substitutions of model structures are widely applied to design the functional materials in solid-state chemistry and crystal engineering. *Im*-3-type KSbO₃ combined with *P*n3 and *R*-3-type KSbO₃ are well-known model structures for the binary oxide materials. Three structural skeletons have a unique and common SbO₆ octahedron unit [1]. The oxide materials consist of a big family with the composition changing from ABO₃ [MSbO₃ (M = Li, Na, K, Rb, Tl, and Ag), KBiO₃, AgBiO₃, BaOsO₃, and KIrO₃] [2–6], to ABO₃.₅ (Bi₃Ge₃O₁₀.₅) [7] and ABO₃.₆₆₇ (Bi₃GaSb₂O₁₁, Bi₃AlSb₂O₁₁, Bi₂NaSb₃O₁₁, Bi₃Ru₃O₁₁, La₃Ru₃O₁₁, and Bi₃Mn₃O₁₁) [8–13]. A large number of novel properties were harvested by the isomorphous substitution of cations, such as the photocatalysis of bismuthates [14,15], the electrocatalysis of ruthenates [16], the photoluminescence of germanate [7], and the ion conductivity of alkali metals [3,17], etc. In order to investigate the ionic tolerance and structural stability for these model structures, we employ the pressure variable to probe the structural adjustment as isomorphous substitutions. In this work, high pressure *in situ*

X-ray diffraction and Raman scattering measurements were carried out on the *I*m-3-type KSbO$_3$.

2. Experimental

The body-centered cubic KSbO$_3$ sample used in this study was synthesized with a piston-cylinder apparatus at 2.1 GPa and 800°C for 2 hours, then at 700°C for 4 hours. The specimen was quenched subsequently to room temperature before the pressure release [2]. Analytical grade ilmenite-structured KSbO$_3$ (Sigma-Aldrich) was used as the starting material and sealed in a platinum capsule. The X-ray diffraction lines of the synthesized specimen agree well with the reported body-centered cubic structure (SG: *I*m-3), and accord with the systematic absences of reflection for *h k l* when (*h* + *k* + *l*) is odd [2]. Figure 1 shows the crystal structure viewed along the [111] direction. Pairs of SbO$_6$ octahedron share one edge to form the unit of Sb$_2$O$_{10}$ clusters.

The high pressure experiments were carried out in a symmetric Mao-Bell-type diamond anvil cell [18] with a flat 300-µm culet diamond. A hole with 100 µm diameter and 40 µm thickness was used as the sample chamber, which was drilled at the center of the pre-indented T301 stainless steel gasket. The synthesized cubic KSbO$_3$ crystal was ground to fine powder and pressed into small pellets with the diamond anvils. A KSbO$_3$ pellet and a small ruby chip were loaded into the sample chamber. Two types of pressure-transmitting media Argon and the mixture of Methanol–ethanol–water (16:3:1) were used in experiments.

In situ angular-dispersive X-ray diffraction (ADXRD) experimental measurements were carried out at Beamline 4W2 of BSRF (Beijing Synchrotron Radiation Facility) and Beamline
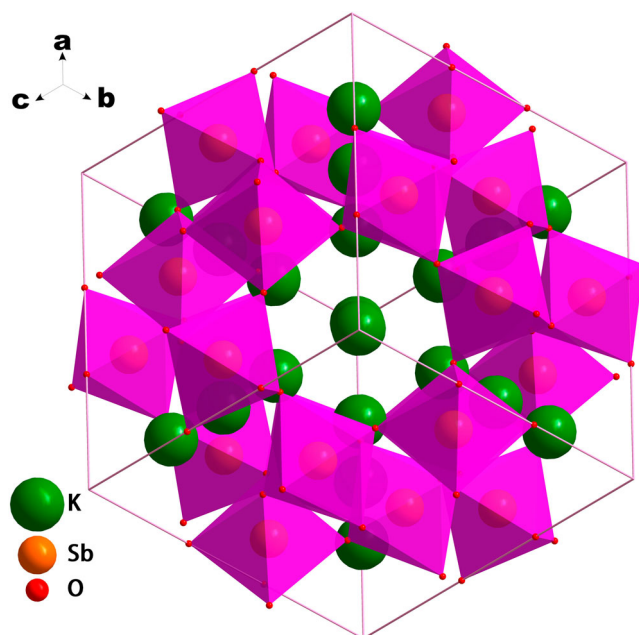

Figure 1. Crystal structure of body-centered cubic KSbO$_3$ viewed along the [111] direction.

15U1 of SSRF (Shanghai Synchrotron Radiation Facility). The X-ray of wavelength 0.6199 Å was used in both Beamlines. The detector in Beamline 4W2 is Mar-345, and in 15U1 is Mar-165. The program Fit2D was used for data analysis. The collected diffraction rings were integrated over the azimuthal angle to obtain a conventional one-dimensional diffraction pattern as intensity vs. diffraction angle 2θ. The pressures of the experiment were calibrated with ruby fluoresce technique [19]. Additional, 1 wt% gold powder was mixed with $KSbO_3$ sample in the experiment of SSRF. The gold was used as pressure scale for *in situ* measurement of the sample pressure [20]. Peak (111) and (200) of gold were mainly used for the pressure calibration. The Rietveld refinements of the ADXRD patterns were carried out using the GSAS-EXPGUI program package [21].

Micro-Raman spectroscopy was measured with an inVia Renishaw spectrometer. A solid laser with the wavelength of 532.4 nm was irradiated to the samples. The size of the laser
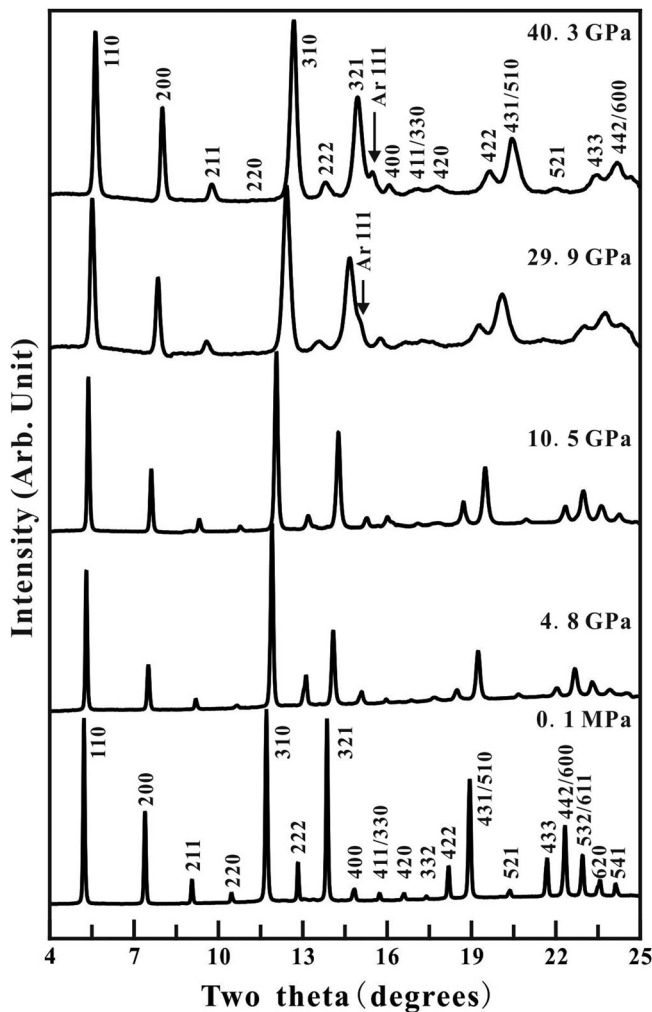

Figure 2. Representative X-ray diffraction patterns of the body-centered cubic $KSbO_3$ at high pressures. In the compression, the peak positions move to higher angles, and the peaks broaden with an increase in pressure. No new additional diffraction peak was observed.

beam was 1–2 µm. Rayleigh scattering light was cut by a Rayleigh filter. Raman spectra were collected with a standard CCD array detector. Each spectrum was collected with the accumulation of two 20-second exposures, *i.e.* the total collection time of each spectrum is 40 (20 × 2) seconds. The wavenumber of the Raman shift was calibrated with single crystalline silicon.

3. Results and discussion

Figure 2 shows the representative ADXRD patterns of the *Im-3*-type $KSbO_3$ from ambient pressure to 40.3 GPa. The patterns of high pressures are similar to that of the starting body-centered cubic structure, although the observed diffraction peaks are obviously broadened and some weak peaks lose their intensity with increase in pressure. In the patterns of 22.9 and 40.3 GPa, the Argon (111) diffraction peak was also observed and marked with

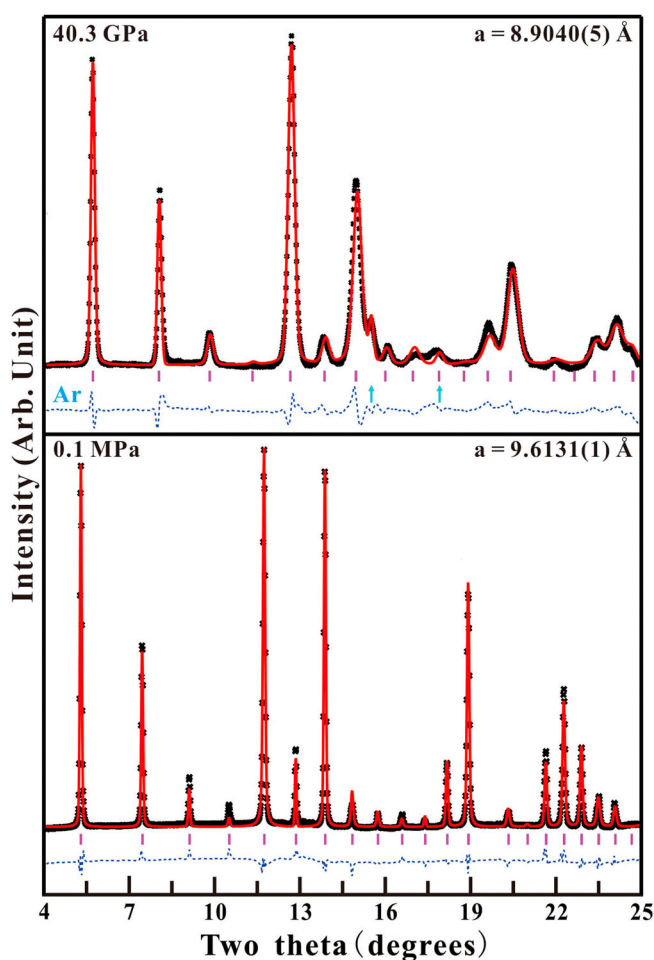**Figure 3.** Rietveld refinement on the X-ray diffraction patterns of $KSbO_3$ at ambient pressure and 40.3 GPa. The observed (crosses), calculated (solid line), and the difference (dotted line) curves are shown on the same scale. Background is subtracted. Tick marks represent the calculated positions of the diffraction peaks of the body-centered cubic $KSbO_3$. The reflections of Ar are indicated by arrows.

an arrow. Figure 3 shows the typical Rietveld refinement patterns at ambient pressure and 40.3 GPa. The initial atomic model was obtained from the reported body-centered cubic structure [22]. Table 1 lists the refined fractional atomic coordinates, unit cell lattice parameters, bond distances, and indices. The good reliability factors of the refinements indicate that the three-dimensional (3D) tunnel structure of $KSbO_3$ remains stable up to 40.3 GPa. Carefully observing the difference curves for the refinement at 40.3 GPa, we found the difference curves corresponding to the 200 and 310 reflections are shifted to a high angle, while those to the 110, 211, 222, and 321 reflections are shifted to a lower angle. Based on the effect of uniaxial stress on the cubic sample [23], it means the stress state was changing worse due to the solidification of pressure-transmitting medium in the diamond anvil cell experiments. The effect of non-hydrostatic stress was also reflected in the broadening of diffraction peaks with the increase of pressure (see Figure 2). Figure 4 shows the relative change of the Sb–O and K–O bonding distances, which was calculated by the formula $(d_{room\ pressure} - d_{high\ pressure})/d_{room\ pressure}$. The linear variation of bonding distances indicates all kinds of Sb–O and K–O bonding except the K2–O2 bonding that has a similar compressibility.

A Birch–Murnaghan equation of state (EOS) was chosen to fit all 51 data points,

$$P = \frac{3}{2}K_0\left[\left(\frac{V_0}{V}\right)^{7/3} - \left(\frac{V_0}{V}\right)^{5/3}\right]\left\{1 + \frac{3}{4}(K'_0 - 4)\left[\left(\frac{V_0}{V}\right)^{2/3} - 1\right]\right\}, \tag{1}$$

Table 1. Structural parameters and refinement indices as determined from the Rietveld analysis of *Im-3*-type $KSbO_3$ at typical pressures.

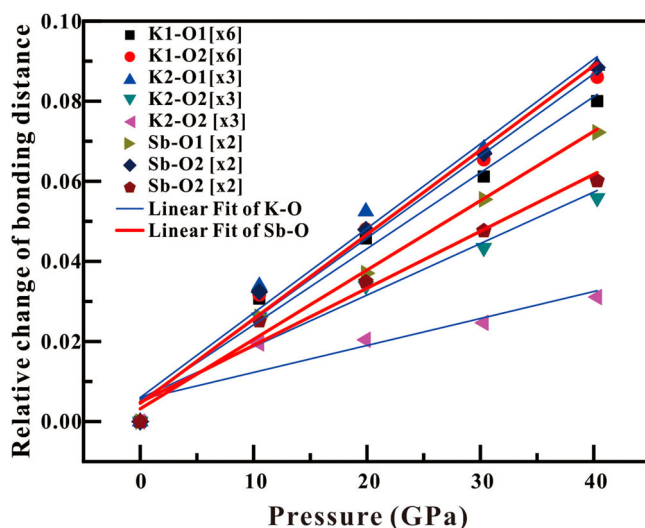| Structural parameters of $KSbO_3$ (*Im-3*, Z = 12) at typical pressures					
	0.1 MPa	10.5 GPa	19.9 GPa	30.3 GPa	40.3 GPa
A	9.6131 (1)	9.3328 (2)	9.2027 (6)	9.0609 (6)	8.9040 (5)
K1 (8c)					
x, y, z	0.25	0.25	0.25	0.25	0.25
K2 (16f)					
x, y, z	0.1459 (7)	0.1429 (4)	0.1389 (8)	0.1356 (6)	0.1323 (8)
Sb (12e)					
X	0.8428 (2)	0.8424 (3)	0.8419 (5)	0.8416 (4)	0.8414 (5)
Y	0	0	0	0	0
Z	0.5	0.5	0.5	0.5	0.5
O1 (12d)					
X	0.3702 (27)	0.3695 (28)	0.3689 (25)	0.3699 (27)	0.3697 (31)
y, z	0	0	0	0	0
O2 (24 g)					
X	0	0	0	0	0
Y	0.3534 (13)	0.3527 (14)	0.3517 (14)	0.3514 (22)	0.3508 (20)
Z	0.2967 (16)	0.2957 (17)	0.2948 (20)	0.2941 (21)	0.2929 (23)
K1–O1 [x6]	3.590 (4)	3.483 (5)	3.433 (4)	3.383 (5)	3.324 (3)
K1–O2 [x6]	2.639 (3)	2.558 (5)	2.518 (4)	2.477 (3)	2.430 (2)
K2–O1 [x3]	2.930 (6)	2.834 (5)	2.784 (6)	2.743 (6)	2.691 (5)
K2–O2 [x3]	2.837 (8)	2.765 (9)	2.744 (9)	2.719 (7)	2.687(7)
K2–O2 [x3]	3.448 (7)	3.382 (5)	3.379 (6)	3.365 (6)	3.344 (6)
Sb–O1 [x2]	1.960 (5)	1.910 (5)	1.890 (4)	1.8573 (5)	1.828 (4)
Sb–O2 [x2]	1.945 (7)	1.884 (6)	1.856 (5)	1.823 (6)	1.787 (6)
Sb–O2 [x2]	1.957 (6)	1.909 (5)	1.891 (7)	1.868 (6)	1.846 (5)
Refinement indices					
R_{wp}	5.6%	2.9%	9.3%	6.5%	2.6%
R_p	4.2%	1.9%	7.8%	5.0%	1.9%
$R(F)^2$	18.4%	13.0%	19.4%	16.1%	20.3%

Figure 4. The relative change of the bonding distances of the $KSbO_3$ with increasing pressure. The values were calculated by a fractional change of $[(d_{room\ pressure} - d_{high\ pressure})/d_{room\ pressure}]$ in each pressure.

where V_0, K_0, and K_0' are the volume, the isothermal bulk modulus, and pressure derivative of the bulk modulus at zero pressure, respectively. Considering the non-hydrostaticity conditions in the sample chambers, which were induced by the solidification of the pressure media of Argon above 1.4 GPa and methanol–ethanol–water (16:3:1) above 10.5 GPa [24], The parameters of K_0 and K_0' in the third-order Birch–Murnaghan
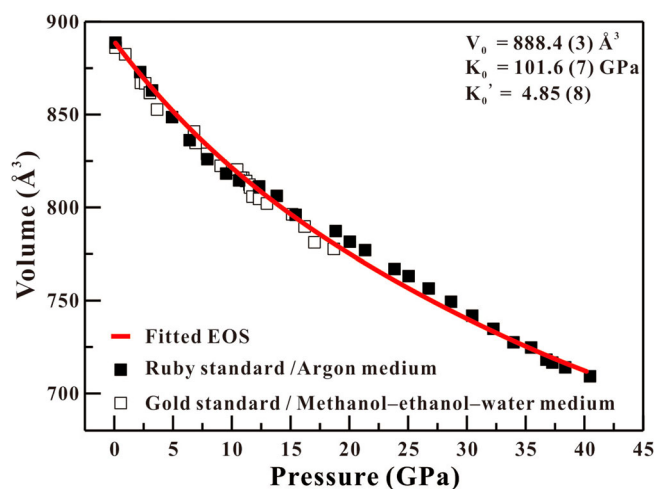

Figure 5. Observed and calculated pressure–volume relationship of $KSbO_3$. Filled and empty squares represent the experimental data with the pressure media of Argon and Methanol–ethanol–water (16:3:1) mixture, respectively. The solid curve is a fit using second-order Birch–Murnaghan EOS. The estimated standard deviations of the unit cell volume (see Table 2) are smaller than the size of the symbols.

EOS were fitted with the fixed zero pressure volume $V_0 = 888.4$ (3) Å^3. We obtained the bulk modulus $K_0 = 101.6$ (7) GPa and its pressure derivative $K'_0 = 4.85$ (8). The bulk modulus of 101.6 (7) GPa was slightly smaller than $K_0 = 109.6$ (8) GPa as a hydrostaticity condition with the $K'_0 = 4$. Figure 5 shows the experimental and calculated unit cell volume of $KSbO_3$ as a function of pressure. The solid line represents the theoretical EOS of Im-3-type $KSbO_3$. The fitted EOS is well in agreement with the empty squares but has a clear deviation to the filled squares. This discrepancy indicates a non-negligible effect of uniaxial stress in the sample chamber with an Argon pressure medium.

The behavior of molecular and lattice vibrations under pressure contains useful information regarding structural stability. In this regard, we also carried out the high pressure Raman measurements on Im-3-type $KSbO_3$. The selected Raman spectra recorded at ambient and high pressures are presented in Figure 6. At the ambient condition, a total of 14 sharp Raman peaks are identified in the range 100–900 cm^{-1}. They are ascribed to the motion of the cations and SbO_6 octahedron units. The internal vibration modes of the SbO_6 octahedron spanned the wavenumber range 450–700 cm^{-1}. The
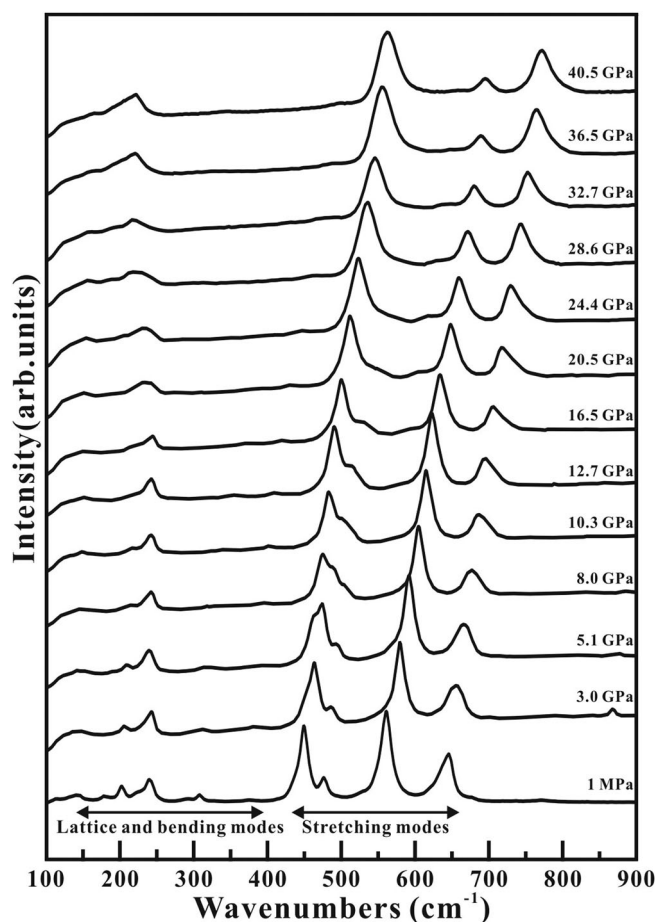

Figure 6. Representative Raman spectra of $KSbO_3$ at ambient and high pressures.

bending vibration modes and the lattice vibration modes of SbO_6 octahedron and KO_{9-12} polyhedron spanned the wavenumber range 100–450 cm^{-1} [25]. According to the relative intensities of the modes in the high and low wavenumber ranges, the Raman modes at 644.7, 634.3, 560.8, 476.2, and 449.4 m^{-1} are assigned to the symmetric and antisymmetric stretching of SbO_6 octahedron. The Raman modes at 435.6, 375.0, 308.8, 240.6, 225.1, 202.6, 179.6, 142.0, and 130.0 cm^{-1} are associated with symmetric bending, antisymmetric bending, and the lattice vibrations of SbO_6 octrahedron and KO_{9-12} polyhedron. Further identification of the Raman modes is difficult owing to the lack of polarized Raman experimental data and theoretical calculations for Im-3-type $KSbO_3$ and other related antimonates. Under high pressures, all modes except the 240.6 cm^{-1} mode shift to higher wavenumbers. The change of Raman intensity for the internal modes is distinctly different with the increase of pressure. For the shoulder peaks 644.7 and 634.3 cm^{-1}, their intensity firstly became weak in the range of 0–16.5 GPa owing to the splitting of the overlapping peaks, then became strong with pressure above 16.5 GPa. The peak of 560.8 cm^{-1} has a marked decrease of intensity in the whole pressure ranges, while the peak 449.4 cm^{-1} maintains its constant intensity to 40.5 GPa. The change of Raman intensity for the internal modes indicates the distortion of SbO_6 octahedron under pressures.

Table 2. The experimental pressure–volume data of Im-3-type $KSbO_3$ using the media of Argon and Methanol–ethanol–water (16:3:1) mixture.

Argon		Methanol–ethanol–water (16:3:1) mixture	
Pressure (GPa)[#]	Volume (Å^3)	Pressure (GPa)[$]	Volume (Å^3)
1 atm.	888.4 (3)	0.1 (1)	885.6 (2)
2.1 (1)	872.8 (4)	0.8 (1)	882.0 (2)
3.1 (1)	862.2 (5)	2.2 (1)	866.4 (3)
4.8 (1)	847.6 (5)	2.5 (1)	866.1 (2)
6.3 (2)	835.0 (3)	2.9 (2)	861.0 (1)
7.8 (2)	824.6 (5)	3.5 (2)	851.8 (2)
9.4 (2)	816.7 (7)	6.7 (2)	839.7 (4)
10.6 (2)	812.9 (3)	6.8 (2)	833.5 (3)
12.2 (2)	809.6 (4)	7.8 (2)	827.5 (3)
13.7 (2)	804.5 (5)	8.9 (2)	820.9 (4)
15.3 (2)	794.1 (6)	10.3 (2)	818.9 (3)
18.7 (2)	785.2 (11)	10.8 (2)	814.3 (2)
19.9 (2)	779.3 (12)	11.1 (2)	812.6 (2)
21.2 (3)	774.7 (14)	11.4 (2)	810.6 (3)
23.7 (3)	764.5 (18)	11.4 (2)	809.0 (4)
24.9 (3)	760.6 (20)	11.6 (3)	804.0 (6)
26.6 (3)	753.9 (23)	12.2 (2)	802.8 (9)
28.5 (3)	746.6 (21)	12.9 (2)	800.3 (8)
30.3 (3)	739.0 (14)	15.0 (2)	794.4 (9)
32.1 (4)	731.8 (24)	16.1 (3)	787.7 (9)
33.8 (4)	724.4 (21)	16.9 (3)	779.0 (11)
35.1 (4)	721.5 (14)	18.6 (3)	775.4 (10)
36.6 (4)	714.8 (10)		
37.1 (4)	713.6 (11)		
38.2 (4)	710.6 (11)		
40.3 (4)	705.9 (11)		

Notes: The estimated standard deviations of the fitted unit cell volume are given in parentheses. The uncertainties of pressure given in parentheses are estimated by the reading uncertainties of the R1 line of Ruby and the reflection peaks (111) and (200) of Gold standard, respectively. The # and $ symbols represent the Ruby and Gold pressure scales, respectively.

Table 3. Observed Raman modes, their pressure dependences (dv_i/dP), and mode Grüneisen parameters γ_i of Im-3-type $KSbO_3$.
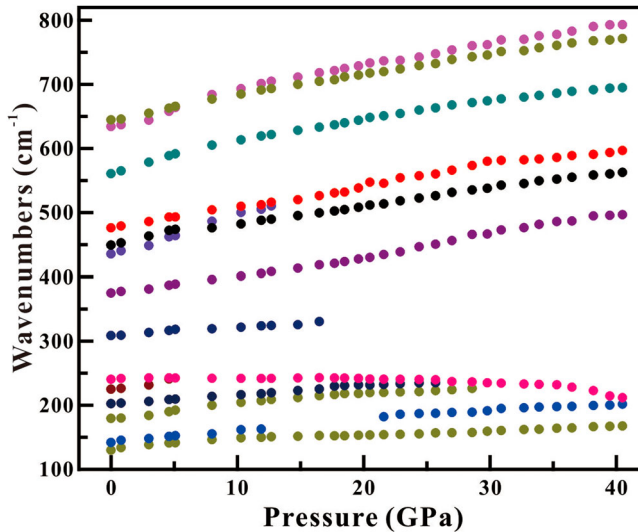
Vibrational mode		Wavenumber (cm⁻¹)			dv_i/dP (cm⁻¹/GPa)	γ_i
		0.1 MPa	20.5 GPa	40.5 GPa		
1	Strong, Shoulder	644.7	717.6	771.5	3.36	0.53
2	Strong, Shoulder	634.3	733.4	793.2	4.32	0.69
3	Strong	560.8	648.4	694.9	3.76	0.68
4	Medium	476.2	547.4	596.9	3.18	0.69
5	Strong, Shoulder	449.4	511.7	562.7	2.95	0.67
6	Weak, Shoulder	435.6	–	–	5.97	1.39
7	Weak	375.0	430.1	496.8	3.00	0.81
8	Weak	308.8	–	–	1.28	0.42
9	Medium	240.6	240.4	212.0	-0.25	-0.11
10	Weak	225.1	–	–	3.04	1.37
11	Medium	202.6	231.6	–	1.38	0.67
12	Weak	179.6	219.8	–	1.87	1.06
13	Weak	142.0	–	201.7	1.62	1.16
14	Weak	130.0	153.6	167.7	1.03	0.80

Notes: Here, dv_i/dP is obtained through a linear fitting of v_i-P data between 0 and 40.5 GPa. The calculated mode Grüneisen parameters γ_i are based on bulk modulus $K_0 = 101.6$ GPa, obtained from this work.

The evolutions of the Raman shifts for the identified modes are shown in Figure 7. All modes except the 240.6 cm⁻¹ mode harden under pressures, although with somewhat different slopes and curvatures. Table 3 lists the observed Raman modes, their pressure dependences (dv_i/dP), and the mode Grüneisen parameters γ_i. The mode Grüneisen parameters were obtained through the below equation:

$$\gamma_i = -\frac{d\ln v_i}{d\ln V} = \frac{K_T}{v_i}\left(\frac{dv_i}{dP}\right), \quad (2)$$

where v_i is the frequency of the ith phonon mode, V is the volume, K_T is the isothermal bulk

Figure 7. Evolution of the Raman shifts with pressure. Solid lines are linear fits to the data in the range 0–40.5 GPa.

modulus at a given pressure, and v and dv/dP are obtained from this study. K_T denotes the value of bulk modulus ($K_0 = 101.6$ GPa) calculated by Equation (1). The internal modes $v_i =$ 644.7, 634.3, 560.8, 476.2, and 449.4 cm^{-1} have similar Grüneisen parameters $\gamma_i = 0.53$, 0.69, 0.68, 0.69, and 0.67, respectively. In contrast, for the modes of bending and lattice vibrations, their Grüneisen parameters are distinctly different; the 240.6 cm^{-1} mode even has a negative value $\gamma_0 = -0.11$. According to Equation (2), similar Grüneisen parameters of internal modes are derived from the equipotent change between the v_i phonon modes of SbO_6 octahedron and the unit cell volume V. This isotropic compress between the internal SbO_6 octahedron and whole unit cell volume ensures that the Im-3-type $KSbO_3$ keeps its original structure under high pressure. It also means that the model Im-3-type $KSbO_3$ structure is stable even with changes in the chemical pressure in the substitutions with various cations.

4. Conclusions

A pure body-centered cubic $KSbO_3$ phase was synthesized at 2.1 GPa and 700–800°C with a piston-cylinder apparatus. *In situ* X-ray diffraction and Raman scattering data show that the 3D tunnel structured $KSbO_3$ remains stable up to 40.5 GPa owing to the isotropic compression for all kinds of the Sb–O bonding in the SbO_6 octahedron. This isotropic compression mechanism reveals the nature why Im-3-type $KSbO_3$ model structure has high structural stability and ionic tolerance while isomorphous substitutions occur.

References

[1] Goodenough J, Hong H, Kafalas J, et al. Research for preparation of cation-conducting solids by high-pressure synthesis and other methods. Final report, 1 Aug 1973–28 Feb 1975. Massachusetts Inst. of Tech., Lexington (USA). Lincoln Lab.; 1975.

[2] Hong H-P, Kafalas J, Goodenough J. Crystal chemistry in the system $MSbO_3$. J Solid State Chem. 1974;9:345–351.

[3] Nguyen TN, Giaquinta DM, Davis WM, et al. Electrosynthesis of $KBiO_3$ (potassium bismuth oxide): a potassium ion conductor with the $KSbO_3$ (potassium antimony oxide) tunnel structure. Chem Mater. 1993;5:1273–1276.

[4] Hoppe R, Claes K. Über oxoiridate: zur kenntnis von KIrO3. J Less Common Metals. 1975;43:129–142.

[5] Sharma R, Mandal TK, Ramesha K, et al. Synthesis and characterization of $AgBiO_3$ with the cubic $KSbO_3$ structure. Indian J Chem. 2004;43A:11–17.

[6] Sarkozy RF, Chamberland BL. The preparation of several new ternary oxides of osmium. Mater Res Bull. 1973;8:1351–1359.

[7] Cheng J, Rettie AJ, Suchomel MR, et al. High-pressure synthesis, structure, and photoluminescence of a new $KSbO_3$-type bismuth germanate $Bi_3Ge_3O_{10.5}$. Inorg Chem. 2013;52:2138–2141.

[8] Kennedy Ismunandar BJ, Hunter BA. Temperature dependent neutron powder diffraction study of $Bi_3(GaSb_2)O_{11}$. Solid State Commun. 1998;108:649–654.

[9] Kennedy Ismunandar BJ, Hunter BA. Structural and surface properties of $Bi_3(MSb_2)O_{11}$ (M = Al, Ga). J Solid State Chem. 1996;127:178–185.

[10] Champarnaud-Mesjard J-C, Frit B, Aftati A, et al. $Nabi_2sb_3o_{11}$: an ordered structure related to the cubic $KSvO_3$ type. Eur J Solid State Inorg Chem. 1995;32:493–504.

[11] Facer G, Elcombe M, Kennedy B. Bismuth ruthenium oxides. Neutron diffraction and photoelectron spectroscopic study of $Bi_2Ru_2O_7$ and $Bi_3Ru_3O_{11}$. Aust J Chem. 1993;46:1897–1907.

[12] Abraham F, Trehoux J, Thomas D. La liaison metal–metal dans les clusters $M_{12}O_{36}$: II—Preparation et etude structurale de la phase $La_3Ru_3O_{11}$. Mater Res Bull. 1978;13:805–810.

[13] Belik AA, Takayama-Muromachi E. $Bi_3Mn_3O_{11}$: a new $KSbO_3$-type random ferrimagnet with high T_c. J Am Chem Soc. 2009;131:9504–9505.

[14] Ramachandran R, Sathiya M, Ramesha K, et al. Photocatalytic properties of $KBiO_3$ and $LiBiO_3$ with tunnel structures. J Chem Sci. 2011;123:517–524.

[15] Ma Z, Wu K, Sun B, et al. Band engineering of $AgSb_{1−x}Bi_xO_3$ for photocatalytic water oxidation under visible light. J Mater Chem A. 2015;3:8466–8474.

[16] He L, Anderson JR, Franzen HF, et al. Electrocatalysis of anodic oxygen-transfer reactions: $Bi_3Ru_3O_{11}$ electrodes in acidic media. Chem Mater. 1997;9:715–722.

[17] Goodenough JB, Park K-S. The Li-Ion rechargeable battery: a perspective. J Am Chem Soc. 2013;135:1167–1176.

[18] Li M-R, Retuerto M, Go YB, et al. Synthesis, crystal structure, and properties of $KSbO_3$-type $Bi_3Mn_{1.9}Te_{1.1}O_{11}$. J Solid State Chem. 2013;197:543–549.

[19] Mao H, Xu J, Bell P. Calibration of the ruby pressure gauge to 800 kbar under quasi-hydrostatic conditions. J Geophys Res. 1986;91:4673–4676.

[20] Dewaele A, Loubeyre P, Mezouar M. Equations of state of six metals above 94 GPa. Phys Rev B. 2004;70:515.

[21] Toby BH. *EXPGUI*, a graphical user interface for *GSAS*. J Appl Crystallogr. 2001;34:210–213.

[22] Goodenough JB, Hong HYP, Kafalas JA. Fast Na^+-ion transport in skeleton structures. Mater Res Bull. 1976;11:203–220.

[23] Takemura K, Dewaele A. Isothermal equation of state for gold with a He-pressure medium. Phys Rev B. 2008;78:235.

[24] Klotz S, Chervin JC, Munsch P, et al. Hydrostatic limits of 11 pressure transmitting media. J Phys D Appl Phys. 2009;42:075413.

[25] Frost RL, Bahfenne S. Raman spectroscopic study of the antimonate mineral brizziite $NaSbO_3$. Radiat Eff Defect Solids. 2010;165:206–210.